Electrochimica Acta 512 (2025) 145425

Contents lists available at ScienceDirect

Electrochimica Acta

journal homepage: www.journals.elsevier.com/electrochimica-acta

Evaluation of high-entropy (Cr, Mn, Fe, Co, Ni)-oxide nanofibers and nanoparticles as passive fillers for solid composite electrolytes

Asia Patriarchi [a,1], Claudia Triolo [b,c,1], Luca Minnetti [a], Miguel Ángel Muñoz-Márquez [a,c], Francesco Nobili [a,c,*], Saveria Santangelo [b,c,*]

[a] Chemistry Division, School of Science and Technology, University of Camerino, 62032 Camerino, Italy
[b] Dipartimento di Ingegneria Civile, dell'Energia, dell'Ambiente e dei Materiali (DICEAM), Università "Mediterranea", Via Zehender, Loc. Feo di Vito, 89122 Reggio Calabria, Italy
[c] National Reference Center for Electrochemical Energy Storage (GISEL), Consorzio Interuniversitario Nazionale per la Scienza e Tecnologia dei Materiali (INSTM), 50121 Firenze, Italy

ARTICLE INFO

Keywords:
High-entropy oxides
Nanofibers
Nanoparticles
Poly(ethylene oxide)
Solid composite electrolytes
Lithium-ion batteries

ABSTRACT

Solid-state electrolytes (SSEs) could represent the key to solve safety issues of lithium-ion batteries (LIBs). Among them, those obtained by homogenously dispersing inorganic nanofillers into a polymer matrix combine advantages of all SSE typologies. In this work, high-entropy (Cr,Mn,Fe,Co,Ni) oxide (HEO) with different morphology (nanoparticles or nanofibers) are evaluated as passive fillers for the preparation of composite polyethylene oxide (PEO)-based SSEs. By varying their preparation conditions (calcination at 400 or 800 °C for 0.5 or 2 h, followed by rapid cooling) different size and crystallization degree of the oxide grains are obtained. The results of the electrochemical testing of the PEO/HEO composites evidence the crucial role of the filler microstructure and morphology. The best results in terms of electrolyte resistance (22.5 Ω), electrochemical stability window (4.7 V), Li^+ transference number (0.37) and ionic conductivity ($3.0 \cdot 10^{-4}$ S cm^{-1} at 65 °C) are obtained by using well crystallized HEO nanofibers with highly defective surface. The suitability of the most promising composite for practical applications is validated by successfully using it in full cell with commercial high-voltage cathode materials.

1. Introduction

Lithium-ion batteries (LIBs) are a key technology to support sustainable mobility and the green transition aimed at helping achieve carbon neutrality by 2050. However, they still suffer from safety issues originating from the use of toxic and flammable liquid electrolytes, featured by poor thermal stability, tendency toward Li dendrite growth and narrow electrochemical voltage window. Solid-state electrolytes (SSEs) could represent the solution to this problem as they promise greater safety.

Among SSEs, solid polymer electrolytes (SPEs) are characterized by high flexibility and compatibility with electrodes, but have poor mechanical resistance and low ionic conductivity [1], whereas inorganic solid electrolytes (ISEs), such as oxides and sulfides, exhibit complementary specifics (high ionic conductivity and good mechanical properties, but poor compatibility with electrodes) [2]. Solid composite electrolytes (SCEs), obtained by homogenously dispersing nano-sized inorganic fillers into the polymer matrix, inherit the advantages from both SPEs and ISEs [3,4].

Nanofillers, such as boron nitride [5], clay montmorillonite[6] and ceramic oxides (e.g. Al_2O_3 [7], ZrO_2 [8], MgO[9], SiO_2[10] or graphitic C_3N_4 [11], simply play a passive role: their incorporation into the polymer matrix inhibits its crystallization disrupting the orderly arrangement of the polymer chains and facilitates their segmental motion [11], thus resulting in composites with improved mechanical strength and ionic conductivity. Li-containing compounds, such as $Li_{10}GeP_2S_{12}$ [12], $Li_7La_3Zr_2O_{12}$ [13], $(Li_2Mg_2O_9Si_3)_3$ [14] and $Li_{0.33}La_{0.557}TiO$ [15] act as active fillers: they provide additional efficient pathways for Li^+ transport with significant enhancement in the ionic conductivity [4,14,15].

Typically, poly(ethylene oxide) (PEO) is the polymer of choice for the preparation of SCEs thanks to its solvation power and superior Li^+

---

* Corresponding authors.
E-mail addresses: francesco.nobili@unicam.it (F. Nobili), saveria.santangelo@unirc.it (S. Santangelo).
[1] A.P. and C.T. contributed equally to this work.

https://doi.org/10.1016/j.electacta.2024.145425
Received 11 October 2024; Received in revised form 22 November 2024; Accepted 26 November 2024

transfer ability of polyethylene oxide chain [16–19]. Several nanostructured materials featured by zero-, one-, two-and three-dimensional architecture, such as BN nanospheres [20], TiO_2 nanotubes[21] and microrods [22], $Bi_4Ti_3O_{12}$ nanofibers [23], ultrathin Co_3O_4 nanosheets [24], BN nanoflakes [25] and nanostructured garnet frameworks [26], have been evaluated as passive fillers to enhance its electrochemical properties. Medium- and high-entropy oxides that take advantage from the cooperative mixing of their multiple metallic components and the synergistic interaction between them [27] have also attracted considerable interest as nanofillers [3,18,28–30].

High ionic conductivity and Li^+ transference number, wide electrochemical window, low electrode/electrolyte interface impedance, high mechanical and thermal stability and low costs are the main requirements that SCEs must meet for their integration in commercial LIBs [1]. The commonly adopted strategy to achieve this goal is to engineer the surface of the inert nanofiller through the activation with hydroxyl groups (OH^-) or the generation of oxygen vacancies (OVs) operated either via an appropriate choice of synthesis conditions [3,28,29] or via post-synthesis treatments [22,24]. According to the widely accepted mechanism [31–34], the strong Lewis acid-base interaction between the surface chemical groups of the inert fillers and the anions from Li salt promotes the salt dissociation, thus contributing to improve Li-ion transport, with ion conductivity and mobility enhancement [35]. The electrochemical stability of SCEs also benefits from Lewis acid-base interaction [31,33,34].

Just to mention a few of cases, Ding et al. [24] have reported that, as a result of the strong adsorption of NO_3^- from $LiNO_3$ electrolyte salt at the defective sites of O-deficient ultrathin Co_3O_4 nanosheets, more Li^+ ions are made available for diffusion and PEO/$Co_3O_{4\text{-}y}$ film reaches a ionic conductivity of $4.9{\cdot}10^{-5}$ S cm^{-1}, a Li^+ transference number of 0.51 and an electrochemical window over 4.6 V at 80 °C. PEO-based SCEs endowed with higher conductivity ($4.28{\cdot}10^{-4}$ S cm^{-1}) are obtained by the use of O-deficient $MoO_{3\text{-}x}$ nanobelts as passive nanofillers [35]. Similarly, OVs on the surface of TiO_2 microrods [22] and of $Bi_4Ti_3O_{12}$ nanofibers, acting as anionic receptors help dissociate lithium bis(trifluoromethansulfonyl) imide (LiTFSI) and promote the rapid transfer of free Li^+ ions, enhancing the electrochemical performance of PEO/LiTFSI electrolytes in which they are incorporated, with polymer/filler interaction further benefiting from the high aspect ratio of the one-dimensional filler architecture.

This paper deals with the synthesis of high-entropy (Cr, Mn, Fe, Co, Ni) oxides (HEOs) to be used as passive fillers in the preparation of PEO/LiTFSI-based SCEs. To the best of the authors' knowledge, this has never been done before. In order to investigate the influence of nanofiller morphology on the electrochemical properties of the resulting PEO/HEO/ LiTFSI SCE, HEOs in the form of nanoparticles (NPs) or nanofibers (NFs) are prepared through sol-gel method (SG) or electrospinning technique (ES), respectively. Calcination is carried out under different conditions (400 °C/ 2 h, 800 °C/ 2 h, or 800 °C/ 0.5 h) to investigate the influence of the oxide grain size and crystallization degree. Based on the commonly agreed concept that enriching the filler surface with OVs or, more generally, with reactive defects (RDs) [20,36] substantially improves the Li^+ diffusion kinetics, in both synthesis routes, calcination is followed by rapid cooling down to room temperature (RT) to generate RDs on the HEO surface [37–39]. The as-prepared HEO NPs and NFs are incorporated into a PEO matrix and the resulting novel SCEs are fully characterized and tested as electrolyte to evaluate their potential utilization with high-voltage cathodes in LIBs.

2. Experimental section

2.1. Synthesis and physicochemical characterization of the HEO fillers

Fillers in the form of nanoparticles (NPs) or nanofibers (NFs) were prepared by sol-gel (SG) method and electrospinning (ES) technique, respectively. A detailed description of the procedures followed for their preparation can be found elsewhere [40]. Briefly, in the case of SG, stoichiometric amounts of Cr, Mn, Fe, Co and Ni salts (Table S1) were dissolved in the solvent, one at a time (Fig. S1a). The gel formed after the addition of the complexing agent under stirring was dried overnight and then calcined in static air (Fig. S1b.1). In the case of ES, the spinnable solution obtained by dissolving metal salts in the polymer/solvent solution, one at a time (Fig. S1a), was loaded in the syringe equipped with a stainless steel needle. ES (Fig. S1b2.1) was operated via a CH-01 Electro-spinner 2.0 (Linari Engineering s.r.l.). Then, the as-spun membrane was lifted off from the collector, dried overnight and calcined in static air (Figure S1b2.2). In both synthesis procedures, temperature was increased at a rate of 10 °C min^{-1} and calcination was followed by rapid cooling down to room temperature (RT) out of the furnace to generate defects on the oxide surface [37–39] and enhance porosity and oxygen deficiency [38]. Since HEOs are usually only thermodynamically stable at elevated temperatures, rapid cooling also ensured that the metastable phase of the material was kinetically trapped [41]. Sample codes and calcination conditions are reported in Table 1. For further details, see Supporting Information (SI).

The physicochemical properties of the fillers were investigated by transmission electron microscopy (TEM), X-ray diffraction (XRD) and micro-Raman spectroscopy (MRS) analyses. A FEI Talos F200S scanning/transmission electron microscope (200 kV) equipped with an EDX spectrometer for elemental mapping was utilized to study morphology and elemental composition. The oxide phase was identified by XRD analysis. A Bruker D2 diffractometer with Ni β-filtered Cu-Kα radiation (λ = 0.1541 nm) was used and diffractograms were analyzed by the Rietveld method using Maud 2.992 software. To assess spatial homogeneity of the fillers, Raman scattering was measured from various random positions on each specimen, using a NTEGRA—Spectra SPM NT-MDT confocal microscope coupled to a solid-state laser operating at 2.33 eV (532 nm). The scattered light was collected by a 100X Mitutoyo objective (NA = 0.75), dispersed by an 1800 lines mm^{-1} grating and detected by a cooled ANDOR iDus CCD Camera. Spectra from different positions were averaged to infer reliable information on the entire sample and fitted to Gaussian bands.

2.2. Preparation of SCEs and electrochemical testing

2.2.1. Materials

Lithium bis(trifluoromethansulfonyl) imide (LiTFSI), poly(ethylene oxide) (PEO, nominal average M_W ~4000,000), conductive carbon (Super C65), N-methyl pyrrolidone (NMP), nickel manganese cobalt oxide (NMC 311) and lithium iron phosphate (LFP) were purchased from Sigma-Aldrich. Solvay supplied Solef polyvinylidene fluoride (PVDF)

2.2.2. Preparation of PEO/HEO/LiTFSI SCEs

PEO/HEO/LiTFSI SCEs were prepared without solvent addition. PEO and LiTFSI were first dried under vacuum overnight in a Buchi oven to remove traces of adsorbed water and then mixed with 10 wt% of HEO filler. Based on previous studies, the selected filler concentration value allows for an optimal balance between improving mechanical properties and maintaining excellent electrochemical performance [21,42–45].

Subsequently, the obtained material was placed between two Teflon sheets and hot-pressed at 70 °C for 2 min to obtain a membrane with a

Table 1
Preparation conditions and filler codes.

Codes		Calcination temperature / °C	Calcination duration / h
Preparation method			
Sol-gel	Electrospinning		
SG400/2	ES400/2	400	2.0
SG800/2	ES800/2	800	2.0
SG800/ 0.5	ES800/0.5	800	0.5

thickness of approximately 150 μm. The resulting blackish membrane was cut into 16 mm disks, dried in a Buchi oven at 50 °C for 15 h and transferred into an argon-filled glove box. The same procedure was used to produce six SCEs, each containing one of the different HEO fillers. The membranes presented good elasticity and tensile strength (Figure S2), in agreement with literature reports [46].

2.2.3. *Preparation of LFP and NMC 311 cathode*

The electrochemical performance of PEO/HEO/LiTFSI SCEs was evaluated both with commercial LFP, which is classically used to evaluate the compatibility between SCEs and cathodic materials, and with commercial NMC 311, in order to test the resistance of the electrolyte when cycled at higher potentials. To prepare the cathode, the active material (80 wt%) was mixed in a mortar with conductive carbon Super C65 (10 wt%) and PVDF binder (10 wt%). NMP was added and the resulting black slurry was stirred gently for 6 h The viscous solution was casted onto an aluminum current collector using a doctor blade (wet thickness 150 μm). Once dried, the laminate was cut into 9 mm disc electrodes (0.636 cm^2 surface, with a mass loading of approximately 3.5 mg cm^{-2}), pressed at 5 ton for 30 s and further dried in a Buchi oven at 120 °C for 4 h Finally, the electrodes were placed in an Ar-filled glove box.

2.2.4. *Characterization PEO/HEO/LiTFSI SCEs*

A Zeiss Sigma 300 FE - SEM was used to investigate the SCE morphology and the distribution of LiTFSI and HEO fillers within it. Thermal gravimetric analysis (TGA) was conducted in the 30–500 °C temperature range under N_2 atmosphere, with a heating rate of 10 °C min^{-1}, utilizing a PerkinElmer STA6000 TGA-DTA instrument.

The electrochemical tests were performed using 9 mm disc electrodes and 16 mm disc electrolyte membranes in CR2032 coin-type cells assembled in an argon-filled glovebox (Jacomex GP Campus with O_2 and H_2O levels < 0.8 ppm). In order to investigate the conductivity of the SCEs, potentiostatic electrochemical impedance spectroscopy (PEIS) was performed at 65 °C in a symmetrical Li/SCE/Li cell configuration (frequency range from 101 kHz to 5 mHz).

Ionic conductivity (σ) was determined by means of impedance spectroscopy in the frequency range from 101 kHz to 5 mHz, with impedance spectra recorded at 5 °C intervals 25–65 °C temperature range. The SCE was placed in a custom-made Teflon O-ring to ensure a uniform thickness of electrolyte and to avoid changes at different temperatures. Conductivity tests were performed in a symmetrical stainless steel (SS)/SCE/SS cell configuration.

For the characterization of transport properties, and determination of Li^+ transference number, Bruce-Vincent-Evans method was used in a lithium symmetric cell configuration (Li/SCE/Li). An impedance spectrum (frequency range from 101 kHz to 5 mHz) was recorded before and after a chronoamperometry (CA) measurements applying a voltage of 90 mV for 60 min.

The anodic stability window of the electrolytes was determined by means of linear sweep voltammetry (LSV) and CA. For this purpose, Super C65 was mixed with PVDF in a mass ratio of 8:2 to form a mixture that was then poured onto an aluminum foil. Once dried, the laminate was cut into 9 mm disc electrodes and used as working electrode (WE) in a Li/SCE/WE cell configuration for the determination of the electrochemical stability window. Linear sweep voltammetry and chronoamperometry measurements were performed within the OCV-5V potential window. LSV was conducted at a scan rate of 0.1 mV s^{-1}, while for the CA measurements, the potential was held at each step for 1 hour. All the measurements were carried out at 65 °C.

Galvanostatic cycling with potential limitation (GCPL) was conducted to assess the cycling behavior of the most promising solid-state composite electrolyte (SCE). The Li/SCE/LFP cell was initially tested at 1C within the 2.5–4.3 V range for 120 cycles, followed by an evaluation of rate capability in the same voltage window using current densities corresponding to C/10, C/5, C/2, 1C, and C/10 scan rates. Additionally, the Li/SCE/NMC cell was tested at a 1C rate within the 2–4.5 V window.

3. Results and discussion

3.1. *Physicochemical properties of fillers*

As shown in previous studies, [40,47] SG method leads to the formation of agglomerates of NPs with broadly distributed size (Fig. 1a-c, g-i). The NP size strongly depends on calcination conditions and increases in the order SG400/2 << SG800/0.5 < SG800/2, as expected.

Straight NFs are obtained by ES (Figure S3). Those calcined at 400 °C are 3–5 μm long and look smooth (Fig. S3a), while NFs calcined at 800 °C exhibit broadly distributed lengths and granular architecture (Figure S3b,c). Higher magnification images (Fig. 1d-f) reveal that all fibers consist of space-confined interconnected oxide grains, which form during the thermal treatment, upon the opposite solicitations experienced from the precursor NF components (expansion of the polymer and contraction of the embedded metal-acetate network), due to degradation of their organic components [48–50]. This results in the formation of copious lattice defects and unsaturated metal sites on the metal oxides [40]. The defects are mainly located at the nanograins connection interface [36,45]. Being richer in grain boundaries, the nanograins forming electrospun NFs are richer in (therein located) defects compared to NPs produced by SG. Similar results were previously found for HEOs based on a different metal combination and having a different lattice structure [51], which suggests that this is a general behavior.

The size of the polyhedral grains forming the fibers varies in the same order as that of NPs (ES400/2 << ES800/0.5 < ES800/2), but is slightly smaller than that of NPs produced by SG method under the same calcination conditions, in line with previous studies [40,50]. ES400/2 NFs are made up of tiny grains (Fig. 1j), which give them the smooth appearance (Figure S3a) [52,53], while ES800/0.5 and ES800/2 NFs are composed of larger particles (Fig. 1k,l). Sintering effects occurring at higher calcination temperature are responsible for both the increase in oxide grain size and formation of an inner cavity resulting in hollow NFs [54].

Elemental mapping via STEM/EDX (Fig. 1m,n) proves the spatially uniform distribution of Cr, Mn, Fe, Co, Ni and O throughout all samples.

Fig. 2 displays the results of XRD and MRS analyses. Very broad diffraction features are detected in the patterns of fillers calcined at 400 °C (Fig. 2a,b), which reflects the smaller size of the oxide grains. Apparently, regardless of the preparation method and conditions, only reflections from the crystalline planes of the spinel structure (JCPDS no 22–1084) seem to be present in the diffractograms of all fillers [40,50, 55–60]. Nonetheless, Rietveld refinements from XRD data (Figure S4) reveal that, regardless of the synthesis route, at 400 °C, part of Cr, Mn, Fe, Co and Ni segregates into a secondary phase with rock-salt (RS) structure (*Fm-3m* space group); the relative amount of this phase (Table S2) is larger in sample SG400/2 (22.6 % against 8.4 % in ES400/2). Conversely, pure single-phase spinel oxide (*Fd-3m* space group) is obtained at 800 °C. At this temperature, larger HEO crystallites form (Table S2), as expected [61,62]. In all samples, the crystallite size (d_{HEO}) is comparable to the size of the oxide grains (Fig. 1e,f), indicating that NPs and grains that form the NFs are mainly single crystals.

MRS provides complementary information. Thanks to the size of the region probed (< 0.6 μm^2), it allows evaluating the spatial homogeneity of the fillers in terms of phase(s) formed. Fig. S5 displays the spectra measured from several random locations on each filler. Except for samples SG400/2 (Fig. S5a) and ES800/0.5 (Fig. S5e), comparing the spectral profiles recorded at different locations, no significant differences are noted, which indicates the spatial uniformity of the phase(s) formed. The differences observed at some locations in SG400/2 might be due to the presence of RS-structured nanodomains organized in larger clusters (Table S2), while broader features and higher photoluminescence background in some locations of ES800/0.5 would

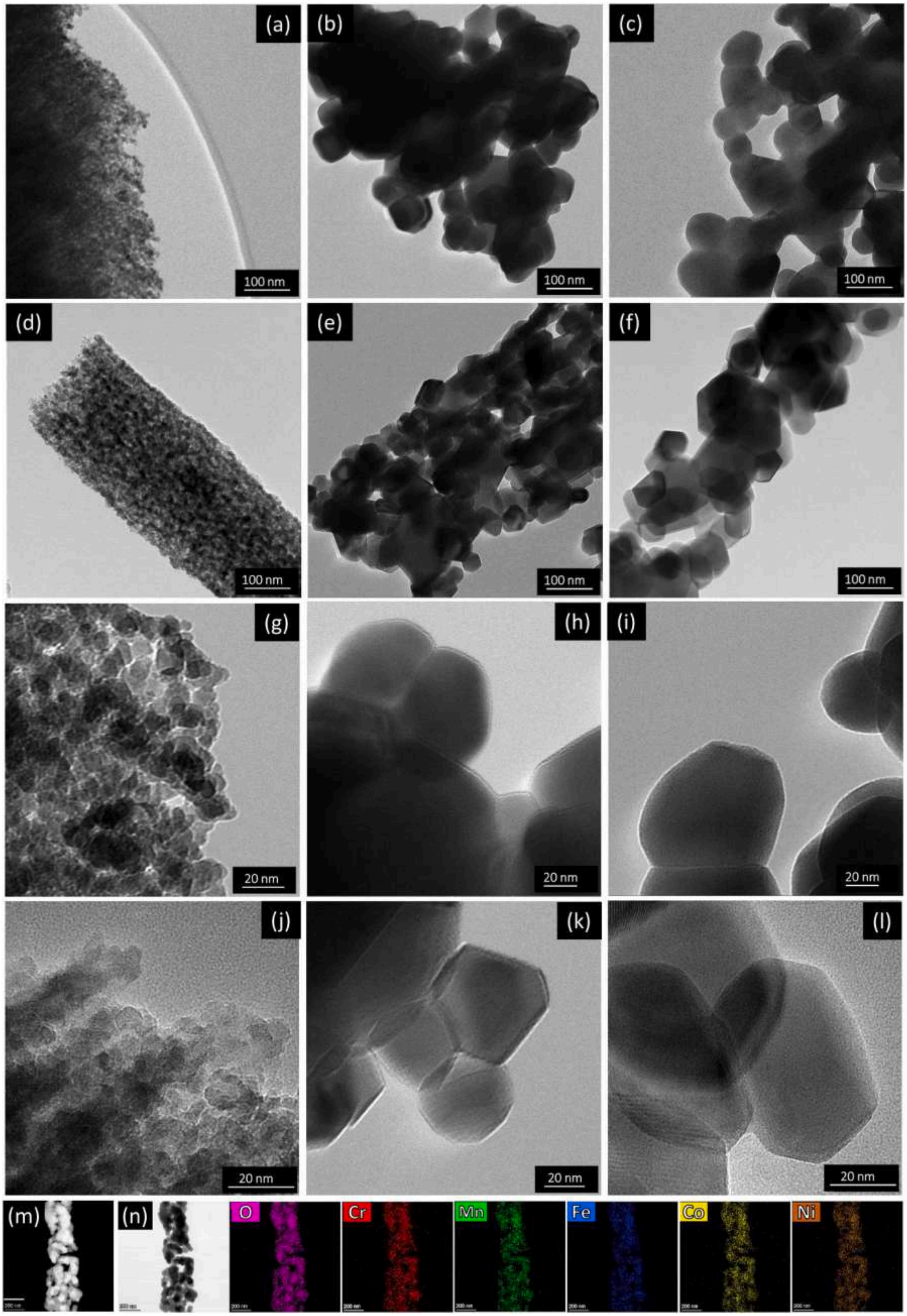

Fig. 1. (a-f) TEM and (g-h) TEM images of fillers (a,g) SG400/2, (b,h) SG800/0.5, (c,i) SG800/2, (d,j) ES400/2 (e,k) ES800/0.5 and (f,l) ES800/2. (m) BF-STEM and (n) HAADF-STEM image of filler ES800/2 followed by the corresponding elemental maps.

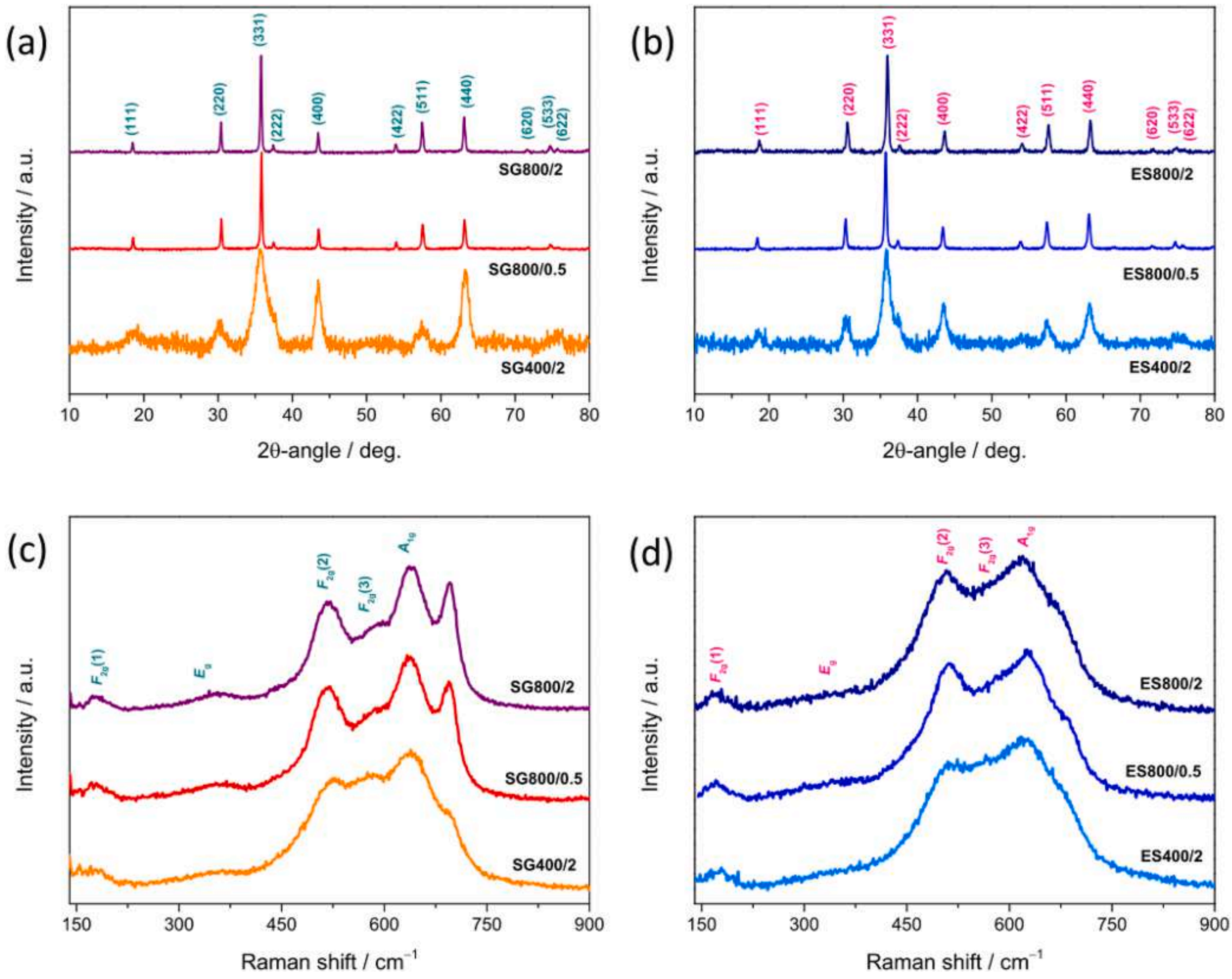

Fig. 2. (a,b) XRD patterns and (c,d) averaged micro-Raman spectra of the fillers produced by (a,c) SG method and by (b,d) ES technique.

indicate that more-defective regions are present in its spinel lattice. Rapid cooling after calcination at higher temperature (800 °C) results in greater thermal shock and is more effective in generating defects on less crystallized samples (calcined only for 0.5 h) [37–39]. Thus, regardless of the preparation method, the density of defects is expected to increase in the order 400 °C/2 h << 800 °C/2 h < 800 °C/0.5 h.

Information about the degree of crystallinity and inversion of the spinel (component of the) oxide can be inferred from the average spectra shown in Fig. 2c,d. An in-depth discussion on Raman scattering from spinel-structured HEOs can be found in ref. [40]. Briefly, five Raman-active normal vibration modes ($A_{1g} + E_g + 3F_{2g}$) are predicted for the spinel lattice [63–65] with strongly varying frequency positions and relative intensities [57,66–71].

Features in the spectra of fillers produced by SG, and particularly of those calcined at 800 °C, are better resolved, as expected due to the larger grain/crystallite size. The spectra of SG800/0.5 and SG800/2 (Fig. 2c) are very similar to those (Cr, Mn, Fe, Co, Ni) HEO NPs prepared through the solid-state reaction [69] and the reverse co-precipitation approach [68]. Only the Raman fingerprint of the spinel oxide is clearly visible in all spectra. Nevertheless, the spectra fitting to Gaussian bands (Figure S6a-f) reveals that, beside to the normal phonon modes of the spinel lattice, inversion-induced modes also contribute to the Raman intensity in all samples [50,64,66,68,69]. In addition, the most intense phonon mode of the RS phase (at 550 cm^{-1}) is identified in SG400/2 and ES400/2 (Figure S6a and d, respectively). The relative intensity of this band in the two fillers (Fig. S6g) agrees with the relative amounts of the RS phase resulting from Rietveld refinements (Table S2). The A_{1g}'/A_{1g} band intensity ratio *qualitatively* monitors the inversion degree of the spinel lattice. [50] Regardless of the preparation method, higher values are obtained for fillers calcined at higher temperature/for longer time (Fig. S6g), as expected based on the evolution of the metal cation distribution promoted by the variation of the calcination conditions previously proposed (Fig. S7) [50,66].

3.2. Membrane characterization

The synthesized SCEs appear like a black, self-standing film with a thickness of approximately 150 μm (Fig. 3**a**). Fig. 3b shows the morphology of the best performing SCE (with ES800/0.5 filler), as resulting from SEM analysis. The membrane surface appears smooth and continuous, without cracks or irregularities. In order to ascertain the homogeneous dispersion of the filler throughout the membrane, which represents a basic requirement for mechanical properties enhancement [46], the electrolyte was further analyzed by SEM/energy-dispersive X-ray spectroscopy (EDX). A fairly homogeneous dispersion of the components of PEO and LiTFSI, namely sulfur (Fig. 3c), oxygen (Fig. 3d), carbon (Fig. 3e) and fluorine (Fig. 3f) is observed (Table S4). The transition metals present in the HEO lattice, namely cobalt (Fig. 3g), nickel (Fig. 3h), chromium (Fig. 3i), manganese (Fig. 3j) and iron (Fig. 3k), are well dispersed too. Except for a slight Cr excess, likely due

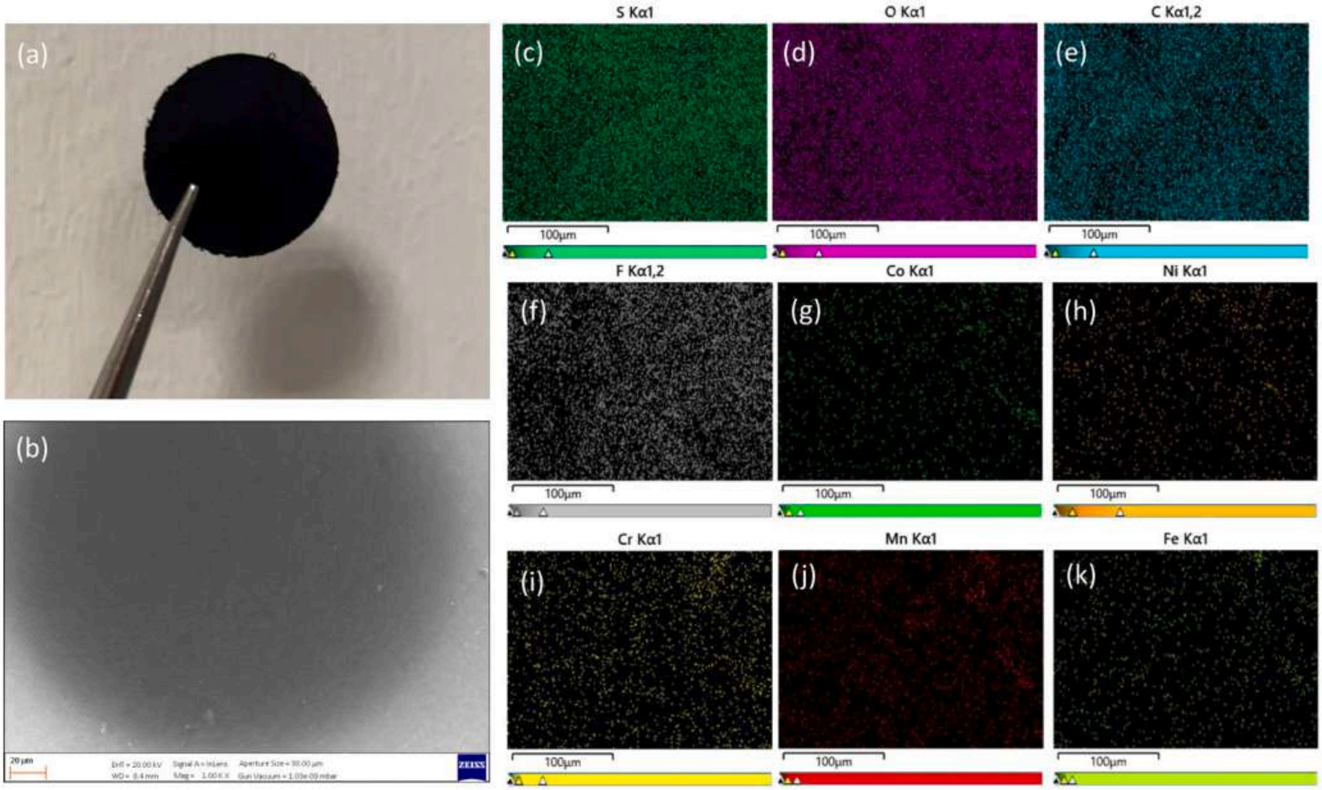

Fig. 3. (a) Photograph and (b) SEM image of the most promising SCE. (c-k) Elemental maps of its components: (c) S, (d) O, (e) C, (f) F, (g) Co, (h) Ni, (i) Cr, (j) Mn, and (k) Fe.

to the metallization of the sample which was performed to increase its electronic conductivity of the electrolyte, the metals are in the stoichiometric atomic ratios.

The thermal stability of the SCEs in the 30–500 °C temperature range was investigated by TGA under nitrogen gas flow. Fig. 4a displays the thermograms of the SCEs incorporating HEO NFs. The lack of significant differences between them indicates that the calcination conditions do not substantially affect the thermal stability of the membrane. The derivative curves (Fig. 4b) allow identifying three main weight losses: the first one (about 2–3 wt%), starting around 60 °C and continuing until 100 °C, is attributed to adsorbed water. The presence of water on the surface of the SCEs is likely the effect of the exposure to air during its preparation: lithium salt and polymer, both hygroscopic in nature, absorb atmospheric moisture. A second weight loss, taking place at around 350 °C, is attributable to the fragmentation of the polymer chains, leading to the formation of lower molecular weight species [72, 73]. A further weight loss is observed in the temperature range (425–445 °C) where the membrane's carbonization may occur [74].

3.3. *Electrochemical properties of PEO/HEO/LiTFSI SCEs*

3.3.1. *Transport and interfacial properties*

The intrinsic resistance of PEO/HEO/LiTFSI SCEs, together with that associated with contact, Li metal interface, double-layer capacitances and Warburg-type bulk solid-state diffusion, was evaluated by means of PEIS (Fig. 5a,b) in a symmetric Li/SCE/Li cells configuration at 65 °C.

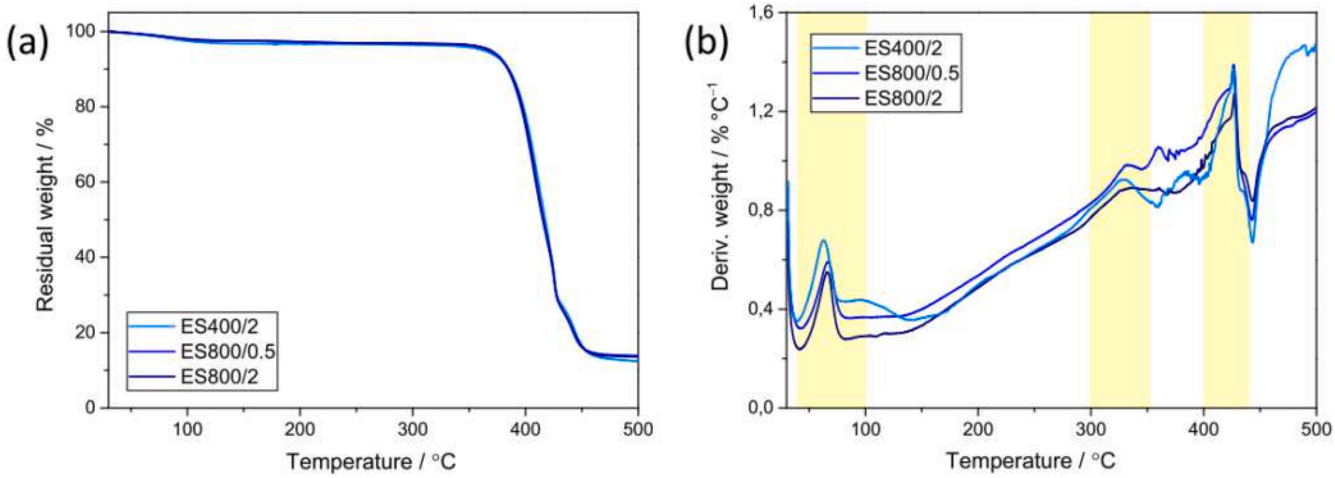

Fig. 4. (a) TGA measurements recorded under nitrogen flow in the 30–500 °C temperature range and (b) relative DTA curves.

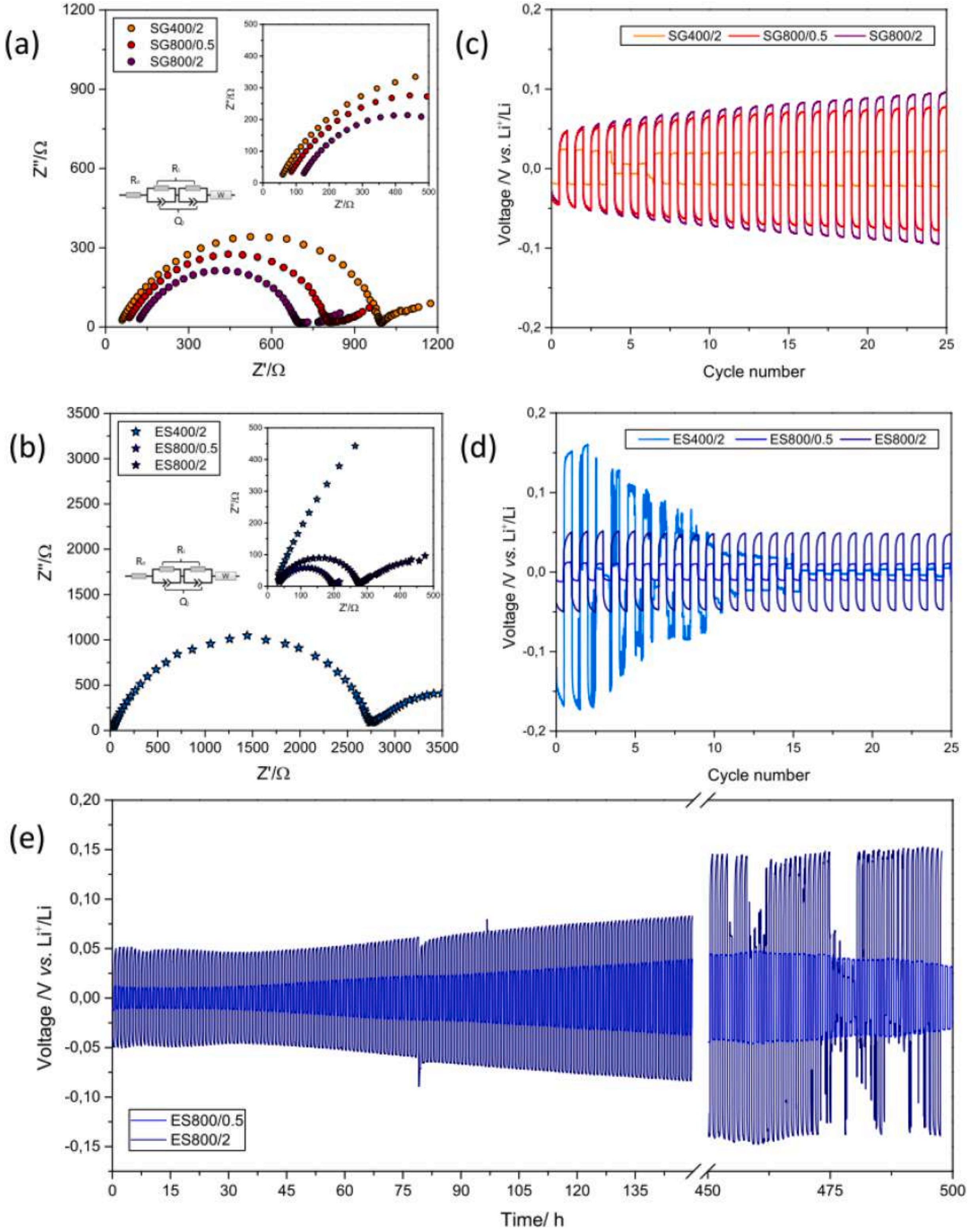

Fig. 5. (a,b) PEIS measurements of PEO-based membranes with HEO fillers prepared by (a) SG and (b) by ES in a symmetric Li/SCE/Li cell at OCV, along with a schematic illustration of the equivalent circuit used for fitting. The inset shows a magnification of the spectra between 0 and 500 Ω. (c,d) Galvanostatic plating/stripping test of symmetrical Li/SCE/Li cells at $T = 65$ °C with a current of 0.05 mA cm^{-2}; for an easier comparison, the same vertical scale is used in the case of SCE containing HEO fillers prepared by (c) SG and (d) by ES. (e) Long cycling performance of SCEs containing 10 % of ES800/2 and ES800/0.5.

The curves were modelled using the equivalent circuit method via NLLS (non-linear least squares) fitting protocol with RelaxIS 3 software. In order to take all contributions into account, the equivalent circuit chosen was Re(RiCi)W (Boukamp's notation), replacing the capacitive elements (C) with a constant-phase element (Q) during fitting to take account of surface imperfections or roughness [75,76]. The resistance values resulting from the fitting process are reported in Table S3. Regardless of the calcination conditions, the use of NFs as fillers leads to a lower intrinsic resistance of the electrolyte (R_E: 22.5–25.6 Ω) compared to NPs (52.9–115 Ω), as better illustrated in the inset of Fig. 5a,b. This clearly points to the crucial role of the filler morphology: NFs facilitate the migration of Li^+ ions through the solid electrolyte by the formation of preferential pathways within which lithium could migrate more efficiently, in line with literature reports [21]. Resulting in better diffusion of Li ions, the formation of tubular or fibrous structures lowers electrolyte resistance to a greater extent than nanoparticles [4, 51,77–79].

Both SG400/2 and ES400/2 fillers exhibited very large values of interphase resistance (R_I: 998 and 2740 Ω, respectively) compared to the fillers calcined at higher temperature. Since at 800 °C the resistance decreases by shortening calcination duration, this behavior is probably due to the enhanced density of surfaces defects [61].

3.3.2. *Stripping and plating tests*

Fig. 5c,d displays the overpotential values obtained by 25 cycles of stripping/ plating tests in Li/SCE/Li symmetric coin cell. When cycled at 0.05 mA cm^{-2}, the membrane containing the 10 % of ES800/0.5 shows the lowest and the most stable overpotential, in agreement with the small R_E and R_I values obtained by PEIS measurements. Conversely, the worst performance pertains to the SCE endowed with the highest R_I value (ES400/2): the latter SCE displays inadequate cycling performance, with dendrite formation as early as the second cycle, leading to the cell short-circuit within a short time. By comparing SCEs containing ES800/0.5 and ES800/2 fillers (Fig. 5e), it comes into view that the overpotential of the former is lower and remains fairly constant over time, while that of the latter increases significantly during the 500 stripping/plating cycles. This behavior hints at the beneficial effect of shortening calcination duration to increase surface defects. As previously reported in literature, the surface defects, produced by the thermal shock experienced by the filler upon post-calcination cooling, may enhance Li^+ transport and suppress Li dendrite formation, contributing to stable cycling performance [80].

3.3.3. *Electrochemical stability window*

The anodic stability window of the electrolytes was investigated in a Li/SCE/WE cell configuration by means of LSV. Fig. 6a compares the current response to the rising potential of the investigated SCEs. In the first region of the curve, the current recorded, close to zero, slightly increases linearly with potential due to the movement of the $TFSI^-$ anion [81]. Above 4 V, the SCE containing 10 % of ES400/2 filler exhibited a marked increase in current, likely due to oxidative reactions leading to electrolyte degradation. This finding, together with the results of the

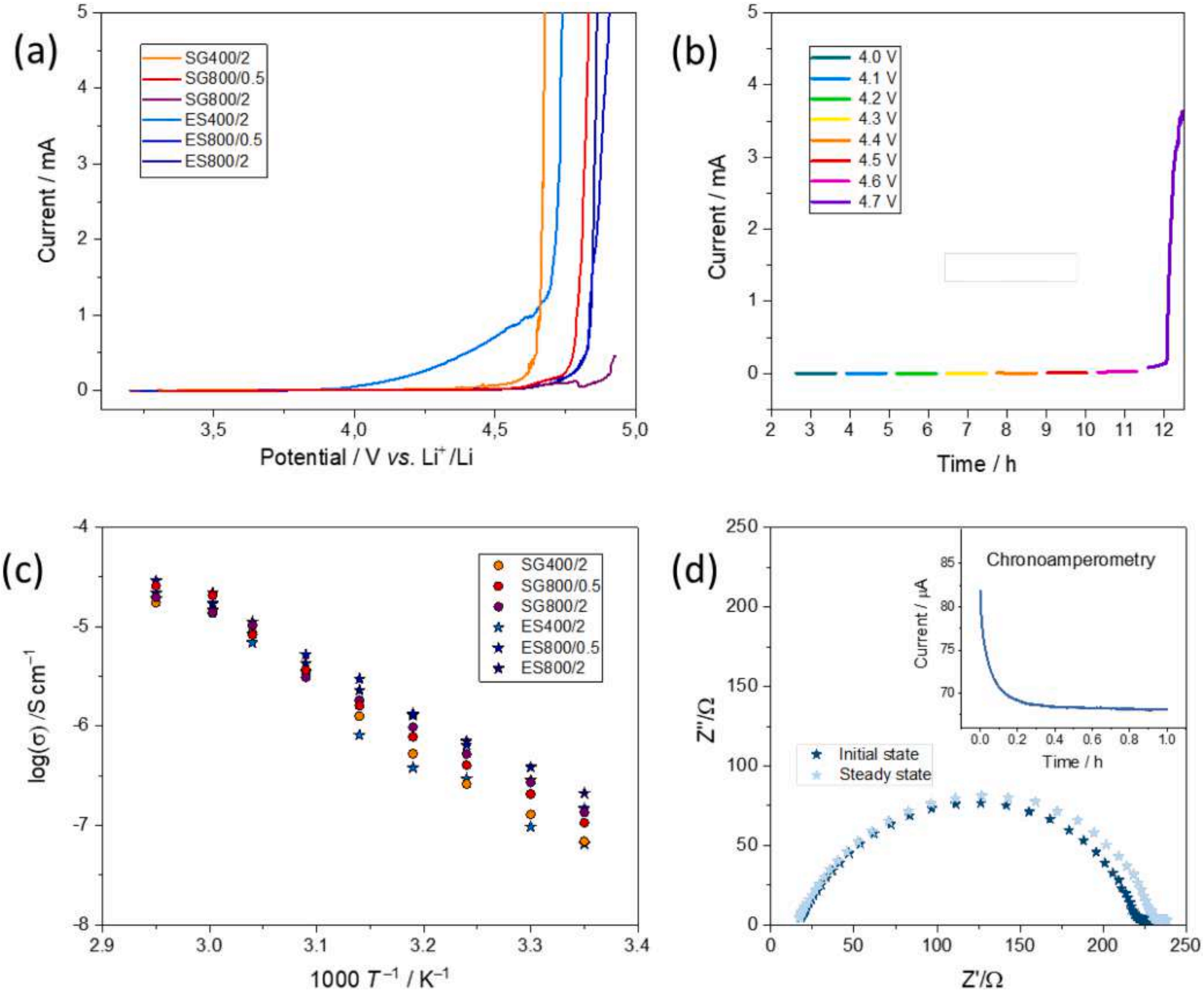

Fig. 6. (a) Linear sweep voltammetry in anodic region performed at 65 °C in Li/SCE/WE cell configuration. (b) chronoamperometry test on Li/ES800 0.5/WE (c) Ionic conductivity plot of the synthesized SCE (d) Nyquist plots used for determining Li^+ transference number at 65 °C of the SCE containing 10 % of ES800 0.5. The inset displays the corresponding chronoamperometry curve.

stripping/plating tests and impedance measurements, further confirms its poor electrochemical performance. The SCE with SG400/2 filler shows a larger stability window, with a significant increase in current only around 4.5 V, a value in line with those reported for PEO /LiTFSI-based polymer electrolytes [21,81,82].

The beneficial effect of the filler addition is evident only for the SCEs containing the fillers calcined at 800 °C, demonstrating a wider stability window up to 4.7 V. According to Chen et al. [3], this improvement results from the stabilizing effect of entropy in the HEO fillers, which prevents the electrolyte from reacting with lithium. The oxidation limit of the most promising SCE was further investigated by carrying out CA measurement within the 4–5 V potential range in a WE/SCE/SS cell configuration (Fig. 6b). In SCE containing ES800/0.5 filler, the threshold for a significant increase in current is 4.7 V. Nonetheless, when the potential is held constant for 1 h, a sharp degradation peak is observed indicating that prolonged system stress leads to degradation of the electrolyte due to polymer oxidation.

3.3.4. *Ionic conductivity*

In the solid-state electrolyte, both anion and cation of the lithium salt dissolved in a polymer matrix can move freely [83]. Li^+ can interact with PEO in the polymer matrix; the formed adducts are essential for the cell conductivity, as they facilitate the passage of lithium through a coupling/decoupling mechanism of the Li-O bond. In particular, the dissociation energy of Li-O bonds and the mobility of the polymer chains, which can be improved by increasing temperature, are critically important for the mechanism of Li^+ transport within the polymer matrix [84,85]. Moreover, the density of active groups and the molecular structure of the polymer influence the amount of solvated Li^+. Generally, polymers with less dense active groups have fewer Li^+ solvation sites. A good strategy to increase active groups and enhance the free Li^+ content is to incorporate fillers that facilitate the dissociation of LiTFSI, especially those with Lewis acid metal centers [33,34,80] that facilitate the dissociation of LiTFSI and the effective immobilization of $TFSI^-$ anions by RDs on their surface.

The ionic conductivity (σ) of the synthesized SCEs was evaluated by impedance spectroscopy in a SS/SCE/SS cell configuration. Conductivity was determined by fitting the EIS spectra at various temperatures using the R_e (R_1Q_1) equivalent circuit, which accounts for the semicircle associated with grain boundary resistance. This resistance is particularly evident at low temperatures and becomes negligible after the melting point, as illustrated in Figure S8, where the Nyquist plots of the ES800/0.5 SCE are presented. The Arrhenius plot (log σ vs 1000 T^{-1}) displayed in Fig. 6c can be divided into two sections separated by a change in slope between 55 °C and 60 °C: at low temperatures, the electrolyte follows a classic Arrhenius behavior; as the polymer melting temperature is reached (55–60 °C), its behavior is better described by the Vogel-Tamman-Fulcher (VTF) function [86,87]. Above the melting temperature, the liquid-like behavior of the polymer matrix results in a greater degree of freedom for the movement of PEO chains. This reduction in crystallinity and rigidity facilitates the migration of lithium ions [18] and is reflected in more uniform conductivity of SCEs.

Interestingly, both SCEs incorporating electrospun filler calcined at 800 °C exhibit enhanced ionic conductivity especially at lower temperatures, probably due to the high density of defects generated on their surface by thermal shock via rapid cooling and the tubular shape, which provides a preferential path for Li^+ hopping at the electrolyte/filler interface in the SCE [88]. The activation energy required for each SCE has been calculated by the fitting of the Arrhenius plot, as shown in Table S3. The values obtained are generally lower in the case of NFs, in line with previous reports indicating the significant impact of the filler morphology on performance [89–91].

The conductivity trend seems to be also consistent with the Li^+ transference number values (τ^+, Table S3), as calculated using the Bruce–Vincent–Evans method at 65 °C [92]:

$$\tau^+ = \frac{i_{ss}}{i_0} \times \frac{(\Delta V - R_0 i_0)}{(\Delta V - R_{ss} i_{ss})},$$

where i_0 and i_{ss} are the initial and steady-state currents, R_0 and R_{ss} are the initial and steady-state resistances of the passivating layer, and ΔV is the potential applied across the cell.

CA measurements were performed by applying a voltage of 30 mV for 1 h, while PEIS spectra were recorded at the initial and steady-state cell polarization (Fig. 6d). In particular, for electrospun fillers, an increase in τ^+ (from 0.29 to 0.34) is observed when the treatment temperature is raised from 400 to 800 °C while keeping duration constant. Shortening calcination duration from 2 to 0.5 h, while keeping temperature constant, further improves τ^+ to 0.37. An analogous trend is seen in the sol-gel fillers, where τ^+ rises from 0.28 for SG400/2 to 0.33 for SG800/2 and reaches 0.35 for SG800/0.5. These values, in good agreement with previously reported literature findings, prove that the addition of HEOs as fillers generally raises the transference number compared to that of the pure electrolyte which never exceeds 0.28 [21,93,94]. Moreover, this effect seems to be related to the defectiveness generated on the filler surface by the rapid post-calcination cooling process: the greater the density of RDs, the greater the enhancement of τ^+. However, owing to their high aspect ratio, NFs form longer Li^+ conductive pathways at the interface with the polymer matrix. It can be envisaged that in SCE containing ES400/2 NFs with lower RD density, $TFSI^-$ anions immobilized on the filler surface are not enough to change appreciably the ionic conductivity; thus, *mainly* random Li^+ hopping occurs, without any significant contribution from the filler other than fragmentation of the polymer chain (Fig. 7a). On the contrary, in SCEs containing ES800/2 and ES800/0.5 NFs with highly defective surface, Li salt dissociation with $TFSI^-$ anion immobilization at surface RDs results in additional (free Li ions and) effective channels for Li^+ hopping (Fig. 7b).

Finally, the electrochemical behavior of the best performing (PEO/ES800/0.5/LiTFSI) SCE was compared with that of the pristine electrolyte (PEO/LiTFSI). The comparison between the key characteristics of the two electrolytes (Fig. S9) demonstrates that the incorporation of HEO within PEO/LiTFSI electrolyte has a beneficial impact on the interfacial membrane/lithium metal properties, as it results in reduced R_E and R_O resistances (Fig. S9a). This improvement is further evidenced by a decrease in overpotential, contributing to greater stability during repeated stripping and plating cycles (Fig. S9b). Moreover, the filler inclusion in the PEO matrix significantly extends the anodic stability window of the electrolyte, as shown in Figure S9c. The PEO/LiTFSI membrane begins to degrade at 4.4 V, while the PEO/ES800/0.5/LiTFSI membrane maintains negligible current at the same voltage, indicating superior stability. This improvement highlights the effectiveness of the SCE design in improving both the electrochemical and interfacial properties of the electrolyte. Finally, the pristine electrolyte exhibits a significantly lower lithium-ion transference number compared to the SCE (Figure S9d). This finding further confirms the critical role of reactive defects on the filler surface; by promoting a more efficient lithium salt dissociation and immobilizing the $TFSI^-$ anion, thereby facilitating lithium mobility within the polymeric matrix, they contribute to enhance τ^+.

3.3.6. *Lithium metal/SCE/LFP full cell*

The performance of the most promising solid-state electrolyte (i.e. the composite of PEO, LiTFSI and ES800/0.5 filler) was evaluated at 65 °C in a full cell configuration using lithium metal as the anode and LFP as the cathode material. The galvanostatic discharge/charge profiles (Fig. 8a) and cycling trend (Fig. 8b) demonstrate a quite stable performance at 1C (170 mA g^{-1}) with a specific capacity of approximately 155 mAh g^{-1}. Within the 2.5–4.3 V potential range, the Li/SCE/LFP cell profile is characterized by a plateau at 3.45 V, due to the presence of the Fe^{3+}/Fe^{2+} redox couple in LFP. The Coulombic efficiency (CE) of the cell

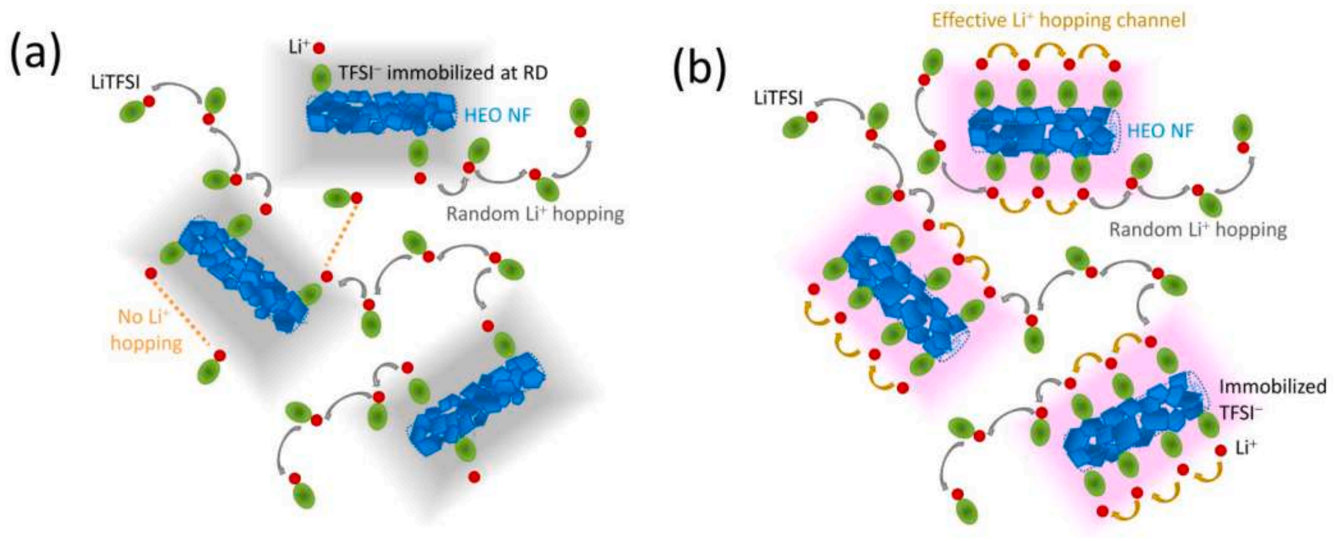

Fig. 7. Schematic illustration of the Li$^+$ hopping in SCE incorporating electrospun NFs with (a) low and (b) high density of surface RDs.

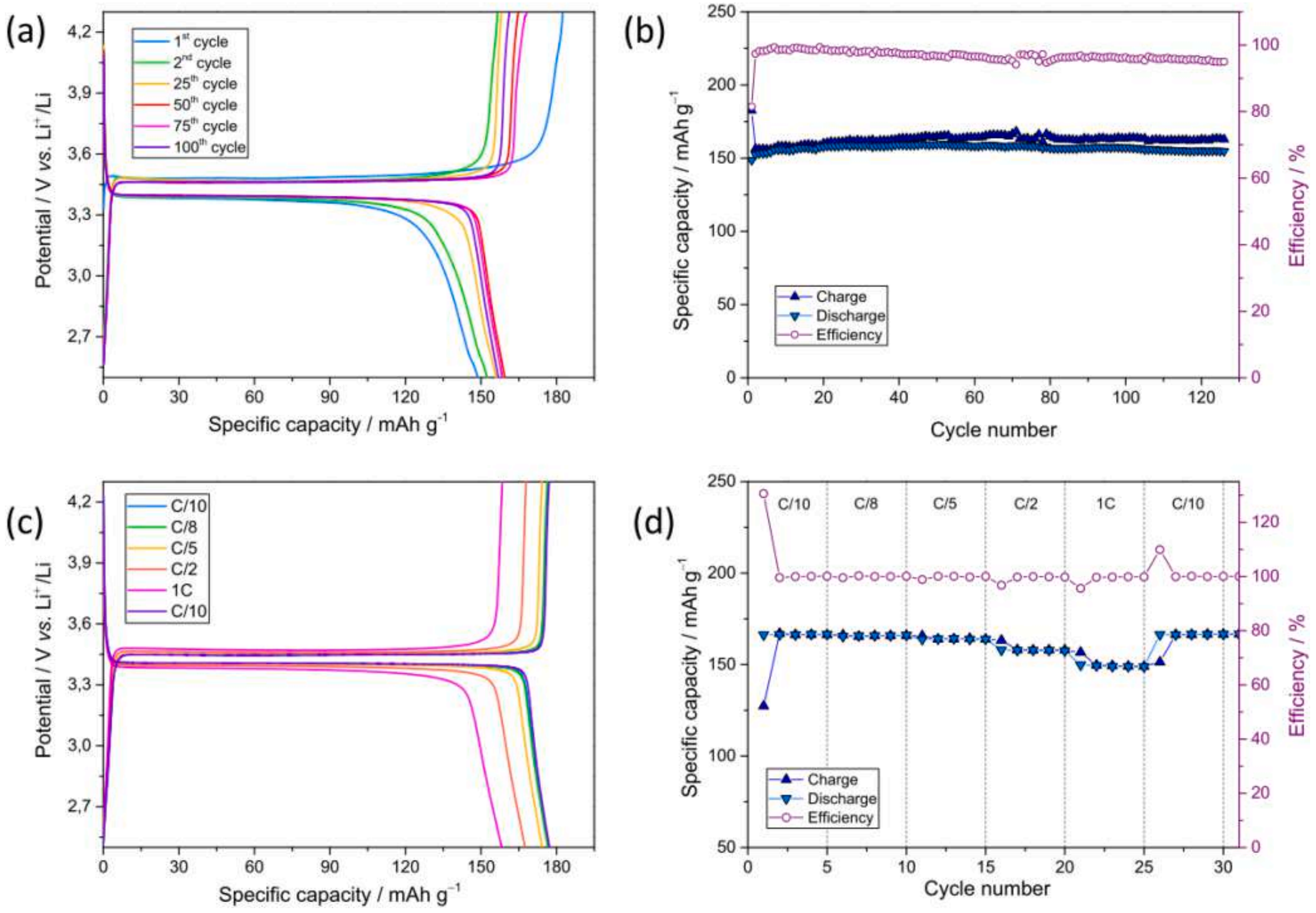

Fig. 8. Electrochemical performance of the cell at constant current rate of 1C in terms of (a) voltage profiles and (b) corresponding cycling trend in terms of discharge capacity and related Coulombic efficiency, within the voltage range 2.5 – 4.3 V. Rate Capability in terms of (c) voltage profiles and (d) corresponding cycling trend performed at C/10, C/8, C/5, C/2 and 1C currents.

is quite high, with values still above 95 % even after 120 cycles and negligible capacity loss. Although a few activation cycles are needed to reach optimum performance (some irreversibility is revealed during first cycle, resulting into higher discharge capacity, lower charge capacity and reduced Coulombic efficiency), as cycling progresses the cell performance increases, probably due to an improved contact between the electrode and the electrolyte.

The tolerance of the cell at different current densities was evaluated by means of rate capability tests (see galvanostatic cell profiles in Fig. 8c). Fig. 8d shows the specific charge and discharge capacity at different current densities and the relative Coulombic efficiency). During the first cycle, the cell does not exhibit optimal electrochemical characteristics probably due to incomplete activation of the material or insufficient contact between electrode and electrolyte. However, after the first cycle, both specific capacity and CE improved. The specific capacity remains almost constant up to currents corresponding to C/2, where a slight increase in polarization in the galvanostatic profile is visible. Remarkably, the capacity of the cell was fully restored by setting the current back to the initial value (C/10), which proves the good stability of the SCE membrane even when subjected to stress, making it suitable for practical applications.

Finally, to evaluate the performance of the SCE at higher potentials, the LFP cathode was replaced with a nickel manganese cobalt oxide cathode and the Li/SCE/NMC 311 was tested in the 3.0–4.55 V potential working window. The membrane showed no failures, no dendrites or dead lithium formation over 50 cycles, with a specific capacity of ~130 mAh g^{-1} and a capacity retention of 88 % after 50 cycles (Figure S10a, b).

4. Conclusions

Several (Cr,Mn,Fe,Co,Ni) HEOs were evaluated as passive fillers for the preparation of PEO/HEO/LiTFSI SCEs for LIBs, with fixed PEO/Li molar ratio (21:1) and HEO content (10 wt%). In order to investigate the effects of the filler morphology (nanoparticles or nanofibers), size and crystallization degree of the HEO grains, fillers were synthesised by different methods (sol-gel and electrospinning, respectively) and both temperature (400 or 800 °C) and duration (0.5 or 2 h) of the calcination process were varied. Thermal shock caused by rapid post-calcination cooling promoted the formation of defects on the HEO surface: the higher the temperature, the shorter the duration, the higher the density of reactive defects.

The lowest electrolyte resistance (22.5 Ω), the largest electrochemical stability window (4.7 V), the highest Li^+ transference number (0.37) and ionic conductivity ($3.0 \cdot 10^{-4}$ S cm^{-1} at 65 °C) are obtained by using HEO nanofibers calcined at 800 °C for 0.5h. The comparative discussion of the results of the filler characterization and SCE electrochemical testing evidence that the morphology and surface defectiveness of the filler mostly influence the SCE performance. Based on the widely accepted Lewis acid-base interaction mechanism, reactive defects at the filler surface promote Li salt dissociation and $TFSI^-$ anion immobilization, while tubular structures provide additional Li^+ hopping pathways, thus both contributing in enhancing Li ion transport.

As proof of concept, the most promising SCE was evaluated in full cell using lithium metal anode and commercial (LFP and NMC 311) cathodes. The results demonstrated good cycling stability, remarkable coulombic efficiency, and excellent tolerance to both high current densities and wide potential windows, indicating its suitability for future practical applications.

CRediT authorship contribution statement

Asia Patriarchi: Writing – original draft, Investigation, Data curation. **Claudia Triolo:** Investigation, Data curation. **Luca Minnetti:** Investigation. **Miguel Ángel Muñoz-Márquez:** Writing – review & editing, Supervision. **Francesco Nobili:** Writing – review & editing, Supervision, Resources. **Saveria Santangelo:** Writing – review & editing, Writing – original draft, Supervision, Resources, Data curation, Conceptualization.

Declaration of competing interest

The authors declare that they have no known competing financial interests or personal relationships that could have appeared to influence the work reported in this paper.

Supplementary materials

Supplementary material associated with this article can be found, in the online version, at doi:10.1016/j.electacta.2024.145425.

Data availability

Data will be made available on request.

References

[1] Y. An, X. Han, Y. Liu, A. Azhar, J. Na, A.K. Nanjundan, S. Wang, J. Yu, Y. Yamauchi, Progress in solid polymer electrolytes for lithium-ion batteries and beyond, Small. 18 (2022), https://doi.org/10.1002/smll.202103617.

[2] C. Cao, Z. Bin Li, X.L. Wang, X.B. Zhao, W.Q. Han, Recent advances in inorganic solid electrolytes for lithium batteries, Front. Energy Res. 2 (2014), https://doi.org/10.3389/fenrg.2014.00025.

[3] Y.T. Chen, J.T. Lee, T.Y. Liang, Y.H. Song, J.M. Wu, Solid composite electrolyte based on oxygen vacancy effect of Lix(CoCrFeMnNi)O4-y high entropy oxides, Electrochim. Acta 456 (2023), https://doi.org/10.1016/j.electacta.2023.142459.

[4] E. Quartarone, P. Mustarelli, A. Magistris, PEO-based composite polymer electrolytes, Solid. State Ion. 110 (1–2) (1998), https://doi.org/10.1016/s0167-2738(98)00114-3.

[5] X.L. Zhang, W.Y. Guo, L. Zhou, Q. Xu, Y. Min, Surface-modified boron nitride as a filler to achieve high thermal stability of polymer solid-state lithium-metal batteries, J. Mater. Chem. a Mater. 9 (36) (2021), https://doi.org/10.1039/d1ta05410d.

[6] Y. Ma, L.B. Li, G.X. Gao, X.Y. Yang, Y. You, Effect of montmorillonite on the ionic conductivity and electrochemical properties of a composite solid polymer electrolyte based on polyvinylidenedifluoride/polyvinyl alcohol matrix for lithium ion batteries, Electrochim. Acta 187 (2016), https://doi.org/10.1016/j.electacta.2015.11.099.

[7] M.K. Wilson, C. Augustin, A. Abhilash, B. Jinisha, A. Antony, M.K. Jayaraj, S. Jayalekshmi, Solid electrolyte membranes with Al2O3 nanofiller for fully solid-state Li-ion cells, Polymer Bulletin 81 (7) (2024), https://doi.org/10.1007/s00289-023-04945-9.

[8] T.K. Lee, A. Ahmad, N. Hasyareeda, Preparation and characterization on nano-hybrid composite solid polymer electrolyte of PVdF-HFP /MG49- ZrO 2 for battery application, AIP. Conf. Proc. (2014), https://doi.org/10.1063/1.4895231.

[9] C. Maheshwaran, D.K. Kanchan, K. Mishra, D. Kumar, K. Gohel, Effect of active MgO nano-particles dispersion in small amount within magnesium-ion conducting polymer electrolyte matrix, Nano-Structures and Nano-Objects 24 (2020), https://doi.org/10.1016/j.nanoso.2020.100587.

[10] A.J. Nagajothi, R. Kannan, S. Rajashabala, Lithium ion conduction in plasticizer based composite gel polymer electrolytes with the addition of SiO2, Materials Research Innovations 22 (4) (2018), https://doi.org/10.1080/14328917.2017.1300725.

[11] J. Li, L. Zhu, H. Xie, W. Zheng, K. Zhang, Graphitic carbon nitride assisted PVDF-HFP based solid electrolyte to realize high performance solid-state lithium metal batteries, Colloids. Surf. a Physicochem. Eng. Asp. 657 (2023), https://doi.org/10.1016/j.colsurfa.2022.130520.

[12] J.A. Dawson, M.S. Islam, A Nanoscale Design Approach for Enhancing the Li-Ion Conductivity of the Li10GeP2S12Solid Electrolyte, ACS. Mater. Lett. 4 (2) (2022), https://doi.org/10.1021/acsmaterialslett.1c00766.

[13] C.K. Chan, T. Yang, J.Mark Weller, Nanostructured Garnet-type Li7La3Zr2O12: synthesis, Properties, and Opportunities as Electrolytes for Li-ion Batteries, Electrochim. Acta 253 (2017), https://doi.org/10.1016/j.electacta.2017.08.130.

[14] L. Zhu, H. Xie, W. Zheng, K. Zhang, Multi-component solid PVDF-HFP/PPC/LLTO-nanorods composite electrolyte enabling advanced solid-state lithium metal batteries, Electrochim. Acta 435 (2022), https://doi.org/10.1016/j.electacta.2022.141384.

[15] J. Li, W. Zheng, L. Zhu, H. Zhou, K. Zhang, Incorporating lithium magnesium silicate into PVDF-HFP based solid electrolyte to achieve advanced solid-state lithium-ion batteries, J. Alloys. Compd. 960 (2023), https://doi.org/10.1016/j.jallcom.2023.170640.

[16] D. Zhang, L. Li, X. Wu, J. Wang, Q. Li, K. Pan, J. He, Research Progress and Application of PEO-Based Solid State Polymer Composite Electrolytes, Front. Energy Res. 9 (2021), https://doi.org/10.3389/fenrg.2021.726738.

[17] W. Hou, Y. Ou, K. Liu, Progress on High Voltage PEO-based Polymer Solid Electrolytes in Lithium Batteries, Chem. Res. Chin. Univ. 38 (2022), https://doi.org/10.1007/s40242-022-2065-2.

[18] T.G. Ritter, J.M. Gonçalves, S. Stoyanov, A. Ghorbani, T. Shokuhfar, R. Shahbazian-Yassar, AlTiMgLiO medium entropy oxide additive for PEO-based solid polymer electrolytes in lithium ion batteries, J. Energy Storage 72 (2023), https://doi.org/10.1016/j.est.2023.108491.

[19] J. Feng, L. Wang, Y. Chen, P. Wang, H. Zhang, X. He, PEO based polymer-ceramic hybrid solid electrolytes: a review, Nano Converg. 8 (2021), https://doi.org/10.1186/s40580-020-00252-5.

[20] J. Ji, C. Liu, Z. Zhou, S. Yan, S. Yang, X. Li, Z. Wang, Y. Xue, C. Tang, Uniform Boron Nitride Nanospheres with Reactive Surface Defects for Composite Solid-State Electrolytes, ACS. Appl. Nano Mater. 7 (2024) 13230–13240, https://doi.org/10.1021/acsanm.4c01757.

[21] A. Patriarchi, H. Darjazi, L. Minnetti, L. Sbrascini, G.A. Elia, V. Castorani, M.Á. Muñoz-Márquez, F. Nobili, All-Solid-State Li-Metal Cell Using Nanocomposite TiO2/Polymer Electrolyte and Self-Standing LiFePO4 Cathode, Batteries. (Basel) 10 (2023) 11, https://doi.org/10.3390/batteries10010011.

[22] B. Luo, W. Wang, Q. Wang, W. Ji, G. Yu, Z. Liu, Z. Zhao, X. Wang, S. Wang, J. Zhang, Facilitating ionic conductivity and interfacial stability via oxygen vacancies-enriched TiO2 microrods for composite polymer electrolytes, Chemical Engineering Journal 460 (2023), https://doi.org/10.1016/j.cej.2023.141329.

[23] J. Kang, Z. Yan, L. Gao, Y. Zhang, W. Liu, Q. Yang, Y. Zhao, N. Deng, B. Cheng, W. Kang, Improved ionic conductivity and enhancedinterfacial stability of solid polymer electrolytes with porous ferroelectric ceramic nanofibers, Energy Storage Mater. 53 (2022), https://doi.org/10.1016/j.ensm.2022.09.005.

[24] Q. Ding, Y. Dou, Y. Liao, S. Huang, R. Wang, W. Min, X. Chen, C. Wu, D. Yuan, H. K. Liu, S.X. Dou, J. Xu, Oxygen Vacancy-Rich Ultrathin Co3O4 Nanosheets as Nanofillers in Solid-Polymer Electrolyte for High-Performance Lithium Metal Batteries, Catalysts. 13 (2023), https://doi.org/10.3390/catal13040711.

[25] J. Shim, H.J. Kim, B.G. Kim, Y.S. Kim, D.G. Kim, J.C. Lee, 2D boron nitride nanoflakes as a multifunctional additive in gel polymer electrolytes for safe, long cycle life and high rate lithium metal batteries, Energy Environ. Sci. 10 (2017), https://doi.org/10.1039/c7ee01095h.

[26] J. Bae, Y. Li, F. Zhao, X. Zhou, Y. Ding, G. Yu, Designing 3D nanostructured garnet frameworks for enhancing ionic conductivity and flexibility in composite polymer electrolytes for lithium batteries, Energy Storage Mater. 15 (2018), https://doi.org/10.1016/j.ensm.2018.03.016.

[27] K. Wang, W. Hua, X. Huang, D. Stenzel, J. Wang, Z. Ding, Y. Cui, Q. Wang, H. Ehrenberg, B. Breitung, C. Kübel, X. Mu, Synergy of cations in high entropy oxide lithium ion battery anode, Nat. Commun. 14 (2023), https://doi.org/10.1038/s41467-023-37034-6.

[28] W. Liu, J. Jiang, Z. Yang, Y. Liu, Z. Yang, M. Bu, S. Liao, W. Wu, T. Huang, S. Sang, H. Liu, Poly(ethylene oxide)-Based Composite Electrolyte with Lithium-Doped High-Entropy Oxide Ceramic Enabled Robust Solid-State Lithium-Metal Batteries, Chem. Asian J. (2022) 17, https://doi.org/10.1002/asia.202200839.

[29] M. Li, L. Wang, Y. Shi, J. Zhang, Q. Zhu, J. Shang, B. Li, S. Yang, High-entropy metal oxide containing hybrid electrolyte for long-life Li-metal batteries, Oxford Open Materials Science 2 (2022), https://doi.org/10.1093/oxfmat/itac011.

[30] Z.P. Cai, C. Ma, X.Y. Kong, X.Y. Wu, K.X. Wang, J.S. Chen, High-Performance PEO-Based All-Solid-State Battery Achieved by Li-Conducting High Entropy Oxides, ACS. Appl. Mater. Interfaces. 14 (2022), https://doi.org/10.1021/acsami.2c18552.

[31] Q. Zhou, J. Ma, S. Dong, X. Li, G. Cui, Intermolecular Chemistry in Solid Polymer Electrolytes for High-Energy-Density Lithium Batteries, Advanced Materials 31 (2019), https://doi.org/10.1002/adma.201902029.

[32] C.H. Park, D.W. Kim, J. Prakash, Y.K. Sun, Electrochemical stability and conductivity enhancement of composite polymer electrolytes, Solid. State Ion. 159 (2003), https://doi.org/10.1016/S0167-2738(03)00025-0.

[33] X. Yang, J. Liu, N. Pei, Z. Chen, R. Li, L. Fu, P. Zhang, J. Zhao, The Critical Role of Fillers in Composite Polymer Electrolytes for Lithium Battery, Nanomicro Lett. 15 (2023), https://doi.org/10.1007/s40820-023-01051-3.

[34] S. Liu, W. Liu, D. Ba, Y. Zhao, Y. Ye, Y. Li, J. Liu, Filler-Integrated Composite Polymer Electrolyte for Solid-State Lithium Batteries, Advanced Materials 35 (2023), https://doi.org/10.1002/adma.202110423.

[35] R. Paste, C. Hanmandlu, P.Y. Su, C.H. Hou, H.A. Chen, C.W. Pao, J.J. Shyue, K. H. Chen, H.L. Wu, H.C. Lin, C.W. Chu, Intimate interaction of TFSI− anions with MoO3−x oxygen vacancies boost ionic conductivity of cathode-supported solid polymer electrolyte, Chemical Engineering Journal 452 (2023), https://doi.org/10.1016/j.cej.2022.139088.

[36] W. Yu, N. Deng, D. Shi, L. Gao, B. Cheng, G. Li, W. Kang, One-Dimensional Oxide Nanostructures Possessing Reactive Surface Defects Enabled a Lithium-Rich Region and High-Voltage Stability for All-Solid-State Composite Electrolytes, ACS. Nano 17 (2023), https://doi.org/10.1021/acsnano.3c07754.

[37] M. Hilal Elhousseini, T. Isık, Ö. Kap, F. Verpoort, N. Horzum, Dual remediation of waste waters from methylene blue and chromium (VI) using thermally induced ZnO nanofibers, Appl. Surf. Sci. 514 (2020), https://doi.org/10.1016/j.apsusc.2020.145939.

[38] A.V. Malyshev, A.B. Petrova, A.N. Sokolovskiy, A.P. Surzhikov, Effect of fast cooling on defects level, microstructure and magnetic properties of LiTiZn ferrite ceramics, Mater. Chem. Phys. 227 (2019), https://doi.org/10.1016/j.matchemphys.2019.02.022.

[39] F. Pantò, Z. Dahrouch, A. Saha, S. Patanè, S. Santangelo, C. Triolo, Photocatalytic degradation of methylene blue dye by porous zinc oxide nanofibers prepared via electrospinning: when defects become merits, Appl. Surf. Sci. 557 (2021), https://doi.org/10.1016/j.apsusc.2021.149830.

[40] B. Petrovičovà, W. Xu, M.G. Musolino, F. Pantò, S. Patanè, N. Pinna, S. Santangelo, C. Triolo, High-Entropy Spinel Oxides Produced via Sol-Gel and Electrospinning and Their Evaluation as Anodes in Li-Ion Batteries, Applied Sciences (Switzerland) 12 (2022), https://doi.org/10.3390/app12125965.

[41] S.S. Aamlid, M. Oudah, J. Rottler, A.M. Hallas, Understanding the Role of Entropy in High Entropy Oxides, J. Am. Chem. Soc. 145 (2023), https://doi.org/10.1021/jacs.2c11608.

[42] W. Wang, E. Yi, A.J. Fici, R.M. Laine, J. Kieffer, Lithium Ion Conducting Poly (ethylene oxide)-Based Solid Electrolytes Containing Active or Passive Ceramic Nanoparticles, Journal of Physical Chemistry C 121 (2017), https://doi.org/10.1021/acs.jpcc.6b11136.

[43] L. Chen, Y. Li, S.P. Li, L.Z. Fan, C.W. Nan, J.B. Goodenough, PEO/garnet composite electrolytes for solid-state lithium batteries: from “ceramic-in-polymer” to “polymer-in-ceramic, Nano Energy 46 (2018), https://doi.org/10.1016/j.nanoen.2017.12.037.

[44] S. Hua, J. lun Li, M. xiang Jing, F. Chen, B. wei Ju, F. yue Tu, X. qian Shen, S. biao Qin, Effects of surface lithiated TiO2 nanorods on room-temperature properties of polymer solid electrolytes, Int. J. Energy Res. 44 (2020), https://doi.org/10.1002/er.5379.

[45] X. Yang, J. Liu, N. Pei, Z. Chen, R. Li, L. Fu, P. Zhang, J. Zhao, The Critical Role of Fillers in Composite Polymer Electrolytes for Lithium Battery, Nanomicro Lett. 15 (2023), https://doi.org/10.1007/s40820-023-01051-3.

[46] M.D. Kiran, H.K. Govindaraju, T. Jayaraju, N. Kumar, Review-Effect of Fillers on Mechanical Properties of Polymer Matrix Composites. Mater. Today Proc., 2018, https://doi.org/10.1016/j.matpr.2018.06.611.

[47] C. Triolo, S. Schweidler, L. Lin, G. Pagot, V. Di Noto, B. Breitung, S. Santangelo, Evaluation of electrospun spinel-type high-entropy (Cr0.2Mn0.2Fe0.2Co0.2Ni0.2) 3O4, (Cr0.2Mn0.2Fe0.2Co0.2Zn0.2)3O4 and (Cr0.2Mn0.2Fe0.2Ni0.2Zn0.2)3O4 oxide nanofibers as electrocatalysts for oxygen evolution in alkaline medium, Energy Adv. (2023), https://doi.org/10.1039/d3ya00062a.

[48] Q. Hu, Z. Wang, X. Huang, Y. Qin, H. Yang, X. Ren, Q. Zhang, J. Liu, C. He, A unique space confined strategy to construct defective metal oxides within porous nanofibers for electrocatalysis, Energy Environ. Sci. 13 (2020), https://doi.org/10.1039/d0ee02815k.

[49] F. Liu, M. Yu, X. Chen, J. Li, H. Liu, F. Cheng, Defective high-entropy rocksalt oxide with enhanced metal−oxygen covalency for electrocatalytic oxygen evolution, Chinese Journal of Catalysis 43 (2022), https://doi.org/10.1016/S1872-2067(21)63794-4.

[50] C. Triolo, K. Moulaee, A. Ponti, G. Pagot, V. Di Noto, N. Pinna, G. Neri, S. Santangelo, Spinel-Structured High-Entropy Oxide Nanofibers as Electrocatalysts for Oxygen Evolution in Alkaline Solution: effect of Metal Combination and Calcination Temperature, Adv. Funct. Mater. 34 (2024), https://doi.org/10.1002/adfm.202306375.

[51] C. Triolo, W. Xu, B. Petrovičovà, N. Pinna, S. Santangelo, Evaluation of Entropy-Stabilized (Mg0.2Co0.2Ni0.2Cu0.2Zn0.2)O Oxides Produced via Solvothermal Method or Electrospinning as Anodes in Lithium-Ion Batteries, Adv. Funct. Mater. 32 (2022), https://doi.org/10.1002/adfm.202202892.

[52] C.Y. Tsay, H.C. Cheng, Y.T. Tung, W.H. Tuan, C.K. Lin, Effect of Sn-doped on microstructural and optical properties of ZnO thin films deposited by sol-gel method, Thin. Solid. Films. 517 (2008), https://doi.org/10.1016/j.tsf.2008.06.030.

[53] S. Santangelo, S. Patanè, P. Frontera, F. Pantò, C. Triolo, S. Stelitano, P. Antonucci, Effect of calcium- and/or aluminum-incorporation on morphological, structural and photoluminescence properties of electro-spun zinc oxide fibers, Mater. Res. Bull. 92 (2017), https://doi.org/10.1016/j.materresbull.2017.03.062.

[54] A. Senthamizhan, B. Balusamy, Z. Aytac, T. Uyar, Grain boundary engineering in electrospun ZnO nanostructures as promising photocatalysts, CrystEngComm. 18 (2016), https://doi.org/10.1039/c6ce00693k.

[55] A. Mao, F. Quan, H.Z. Xiang, Z.G. Zhang, K. Kuramoto, A.L. Xia, Facile synthesis and ferrimagnetic property of spinel (CoCrFeMnNi)3O4 high-entropy oxide nanocrystalline powder, J. Mol. Struct. 1194 (2019), https://doi.org/10.1016/j.molstruc.2019.05.073.

[56] B. Liang, Y. Ai, Y. Wang, C. Liu, S. Ouyang, M. Liu, Spinel-type (FeCoCrMnZn)3O4 high-entropy oxide: facile preparation and supercapacitor performance, Materials 13 (2020), https://doi.org/10.3390/ma13245798.

[57] M. Stygar, J. Dąbrowa, M. Moździerz, M. Zajusz, W. Skubida, K. Mroczka, K. Berent, K. Świerczek, M. Danielewski, Formation and properties of high entropy oxides in Co-Cr-Fe-Mg-Mn-Ni-O system: novel (Cr,Fe,Mg,Mn,Ni)3O4 and (Co,Cr,Fe,Mg,Mn)3O4 high entropy spinels, J. Eur. Ceram. Soc. 40 (2020), https://doi.org/10.1016/j.jeurceramsoc.2019.11.030.

[58] D. Wang, S. Jiang, C. Duan, J. Mao, Y. Dong, K. Dong, Z. Wang, S. Luo, Y. Liu, X. Qi, Spinel-structured high entropy oxide (FeCoNiCrMn)3O4 as anode towards superior lithium storage performance, J. Alloys. Compd. 844 (2020), https://doi.org/10.1016/j.jallcom.2020.156158.

[59] H. Chen, N. Qiu, B. Wu, Z. Yang, S. Sun, Y. Wang, A new spinel high-entropy oxide (Mg0.2Ti0.2Zn0.2Cu0.2Fe0.2)3O4 with fast reaction kinetics and excellent stability as an anode material for lithium ion batteries, RSC. Adv. 10 (2020), https://doi.org/10.1039/d0ra00255k.

[60] T.X. Nguyen, J. Patra, J.K. Chang, J.M. Ting, High entropy spinel oxide nanoparticles for superior lithiation-delithiation performance, J. Mater. Chem. a Mater. 8 (2020), https://doi.org/10.1039/d0ta04844e.

[61] S.W. Oh, H.J. Bang, Y.C. Bae, Y.K. Sun, Effect of calcination temperature on morphology, crystallinity and electrochemical properties of nano-crystalline metal oxides (Co3O4, CuO, and NiO) prepared via ultrasonic spray pyrolysis, J. Power. Sources. 173 (2007), https://doi.org/10.1016/j.jpowsour.2007.04.087.

[62] X. Yin, J. Huang, Z. Pu, J. Li, H. Feng, X. Wang, Y. Wang, Effect of the calcination temperature on the cation distribution and optical properties of Mg0.5Co0.5CrAlO4 spinel pigment, Ceram. Int. 47 (2021), https://doi.org/10.1016/j.ceramint.2021.03.027.

[63] P. Choudhary, D. Varshney, Crystal structure, phonon modes and dielectric properties of 3d Cu2+ ion doped multiferroic Co1-xCuxCr2O4 (x = 0.0, 0.5) chromites, Mater. Res. Express. 4 (2017), https://doi.org/10.1088/2053-1591/aa7e62.

[64] V. D'Ippolito, G.B. Andreozzi, D. Bersani, P.P. Lottici, Raman fingerprint of chromate, aluminate and ferrite spinels, Journal of Raman Spectroscopy 46 (2015), https://doi.org/10.1002/jrs.4764.

[65] H.D. Lutz, B. Müller, H.J. Steiner, Lattice vibration spectra. LIX. Single crystal infrared and Raman studies of spinel type oxides, J. Solid. State Chem. 90 (1991), https://doi.org/10.1016/0022-4596(91)90171-D.

[66] A. Ponti, C. Triolo, B. Petrovičovà, A.M. Ferretti, G. Pagot, W. Xu, V. Di Noto, N. Pinna, S. Santangelo, Structure and magnetism of electrospun porous high-

entropy (Cr1/5Mn1/5Fe1/5Co1/5Ni1/5)3O4, (Cr1/5Mn1/5Fe1/5Co1/5Zn1/5)3O4 and (Cr1/5Mn1/5Fe1/5Ni1/5Zn1/5)3O4 spinel oxide nanofibers, Physical Chemistry Chemical Physics 25 (2023), https://doi.org/10.1039/d2cp05142g.

[67] C. Feng, Y. Zhou, M. Chen, L. Zou, X. Li, X. An, Q. Zhao, P. Xiaokaiti, A. Abudula, K. Yan, G. Guan, High-entropy spinel (FeCoNiMnAl)3O4 with three-dimensional microflower structure for stable seawater oxidation, Appl. Catal. B 349 (2024), https://doi.org/10.1016/j.apcatb.2024.123875.

[68] B. Talluri, K. Yoo, J. Kim, High entropy spinel metal oxide (CoCrFeMnNi)3O4 nanoparticles as novel efficient electrocatalyst for methanol oxidation and oxygen evolution reactions, J. Environ. Chem. Eng. 10 (2022), https://doi.org/10.1016/j.jece.2021.106932.

[69] J. Dąbrowa, M. Stygar, A. Mikuła, A. Knapik, K. Mroczka, W. Tejchman, M. Danielewski, M. Martin, Synthesis and microstructure of the (Co,Cr,Fe,Mn,Ni)3O4 high entropy oxide characterized by spinel structure, Mater. Lett. 216 (2018), https://doi.org/10.1016/j.matlet.2017.12.148.

[70] M.A. Laguna-Bercero, M.L. Sanjuán, R.I. Merino, Raman spectroscopic study of cation disorder in poly- and single crystals of the nickel aluminate spinel, Journal of Physics Condensed Matter 19 (2007), https://doi.org/10.1088/0953-8984/19/18/186217.

[71] Z.Ž. Lazarević, Č. Jovalekić, A. Milutinović, D. Sekulić, V.N. Ivanovski, A. Rečnik, B. Cekić, N.Ž. Romčević, Nanodimensional spinel NiFe2O4 and ZnFe 2O4 ferrites prepared by soft mechanochemical synthesis, J. Appl. Phys. 113 (2013), https://doi.org/10.1063/1.4801962.

[72] M. Jakić, N.S. Vrandečić, I. Klarić, Thermal degradation of poly(vinyl chloride)/poly(ethylene oxide) blends: thermogravimetric analysis, Polym. Degrad. Stab. 98 (2013), https://doi.org/10.1016/j.polymdegradstab.2013.05.024.

[73] K. Pielichowski, K. Flejtuch, Non-oxidative thermal degradation of poly(ethylene oxide): kinetic and thermoanalytical study, J. Anal. Appl. Pyrolysis. 73 (2005), https://doi.org/10.1016/j.jaap.2005.01.003.

[74] S. Faria, C.L. De Oliveira Petkowicz, S.A.L. De Morais, M.G.H. Terrones, M.M. De Resende, F.P. De Frana, V.L. Cardoso, Characterization of xanthan gum produced from sugar cane broth, Carbohydr. Polym. 86 (2011), https://doi.org/10.1016/j.carbpol.2011.04.063.

[75] B.A. Boukamp, A Nonlinear Least Squares Fit procedure for analysis of immittance data of electrochemical systems, Solid. State Ion. 20 (1986), https://doi.org/10.1016/0167-2738(86)90031-7.

[76] B.A. Boukamp, A package for impedance/admittance data analysis, Solid. State Ion. 18–19 (1986), https://doi.org/10.1016/0167-2738(86)90100-1.

[77] B. Scrosati, J. Garche, Lithium batteries: status, prospects and future, J. Power. Sources. 195 (2010) 2419–2430, https://doi.org/10.1016/j.jpowsour.2009.11.048.

[78] F. Croce, G.B. Appetecchi, L. Persi, B. Scrosati, Nanocomposite polymer electrolytes for lithium batteries, Nature 394 (1998), https://doi.org/10.1038/28818.

[79] W. Krawiec, L.G. Scanlon, J.P. Fellner, R.A. Vaia, S. Vasudevan, E.P. Giannelis, Polymer nanocomposites: a new strategy for synthesizing solid electrolytes for rechargeable lithium batteries, J. Power. Sources. 54 (1995), https://doi.org/10.1016/0378-7753(94)02090-P.

[80] Y. Zhu, Q. Zhang, Y. Zheng, G. Li, R. Gao, Z. Piao, D. Luo, R.H. Gao, M. Zhang, X. Xiao, C. Li, Z. Lao, J. Wang, Z. Chen, G. Zhou, Uncoordinated chemistry enables highly conductive and stable electrolyte/filler interfaces for solid-state lithium–sulfur batteries, Proc. Natl. Acad. Sci. u S. a 120 (2023), https://doi.org/10.1073/pnas.2300197120.

[81] J. Qiu, X. Liu, R. Chen, Q. Li, Y. Wang, P. Chen, L. Gan, S.J. Lee, D. Nordlund, Y. Liu, X. Yu, X. Bai, H. Li, L. Chen, Enabling Stable Cycling of 4.2 V High-Voltage All-Solid-State Batteries with PEO-Based Solid Electrolyte, Adv. Funct. Mater. 30 (2020), https://doi.org/10.1002/adfm.201909392.

[82] X. Yang, M. Jiang, X. Gao, D. Bao, Q. Sun, N. Holmes, H. Duan, S. Mukherjee, K. Adair, C. Zhao, J. Liang, W. Li, J. Li, Y. Liu, H. Huang, L. Zhang, S. Lu, Q. Lu, R. Li, C.V. Singh, X. Sun, Determining the limiting factor of the electrochemical stability window for PEO-based solid polymer electrolytes: main chain or terminal -OH group? Energy Environ. Sci. 13 (2020) https://doi.org/10.1039/d0ee00342e.

[83] Y. Zhao, L. Wang, Y. Zhou, Z. Liang, N. Tavajohi, B. Li, T. Li, Solid Polymer Electrolytes with High Conductivity and Transference Number of Li Ions for Li-Based Rechargeable Batteries, Advanced Science 8 (2021), https://doi.org/10.1002/advs.202003675.

[84] A. Mauger, C.M. Julien, Solid Polymer Electrolytes for Lithium Batteries: a Tribute to Michel Armand, Inorganics. (Basel) 10 (2022), https://doi.org/10.3390/inorganics10080110.

[85] Z. Xue, D. He, X. Xie, Poly(ethylene oxide)-based electrolytes for lithium-ion batteries, J. Mater. Chem. a Mater. 3 (2015) 19218–19253, https://doi.org/10.1039/c5ta03471j.

[86] K.M. Diederichsen, H.G. Buss, B.D. McCloskey, The Compensation Effect in the Vogel-Tammann-Fulcher (VTF) Equation for Polymer-Based Electrolytes, Macromolecules. 50 (2017), https://doi.org/10.1021/acs.macromol.7b00423.

[87] A. Maurel, M. Armand, S. Grugeon, B. Fleutot, C. Davoisne, H. Tortajada, M. Courty, S. Panier, L. Dupont, Poly(Ethylene Oxide)−LiTFSI Solid Polymer Electrolyte Filaments for Fused Deposition Modeling Three-Dimensional Printing, J. Electrochem. Soc. 167 (2020), https://doi.org/10.1149/1945-7111/ab7c38.

[88] Y. Zhu, Q. Zhang, Y. Zheng, G. Li, R. Gao, Z. Piao, D. Luo, R.H. Gao, M. Zhang, X. Xiao, C. Li, Z. Lao, J. Wang, Z. Chen, G. Zhou, Uncoordinated chemistry enables highly conductive and stable electrolyte/filler interfaces for solid-state lithium–sulfur batteries, Proc. Natl. Acad. Sci. u S. a 120 (2023), https://doi.org/10.1073/pnas.2300197120.

[89] I.S. Elashmawi, L.H. Gaabour, Raman, morphology and electrical behavior of nanocomposites based on PEO/PVDF with multi-walled carbon nanotubes, Results. Phys. 5 (2015), https://doi.org/10.1016/j.rinp.2015.04.005.

[90] A. Villa, J.C. Verduzco, J.A. Libera, E.E. Marinero, Ionic conductivity optimization of composite polymer electrolytes through filler particle chemical modification, Ionics. (Kiel) (2021) 27, https://doi.org/10.1007/s11581-021-04042-9.

[91] K. Vignarooban, M.A.K.L. Dissanayake, I. Albinsson, B.E. Mellander, Effect of TiO2 nano-filler and EC plasticizer on electrical and thermal properties of poly(ethylene oxide) (PEO) based solid polymer electrolytes, Solid. State Ion. 266 (2014), https://doi.org/10.1016/j.ssi.2014.08.002.

[92] J. Evans, C.A. Vincent, P.G. Bruce, Electrochemical measurement of transference numbers in polymer electrolytes, Polymer. (Guildf) (1987) 28, https://doi.org/10.1016/0032-3861(87)90394-6.

[93] S. Zugmann, M. Fleischmann, M. Amereller, R.M. Gschwind, H.D. Wiemhöfer, H. J. Gores, Measurement of transference numbers for lithium ion electrolytes via four different methods, a comparative study, Electrochim. Acta 56 (2011), https://doi.org/10.1016/j.electacta.2011.02.025.

[94] V. Marangon, Y. Tominaga, J. Hassoun, An alternative composite polymer electrolyte for high performances lithium battery, J. Power. Sources. 449 (2020), https://doi.org/10.1016/j.jpowsour.2019.227508.